Pergamon

PII: S0042-6989(96)00279-9

Vision Res., Vol. 37, No. 10, pp. 1383–1399, 1997
© 1997 Elsevier Science Ltd. All rights reserved
Printed in Great Britain
0042-6989/97 $17.00 + 0.00

Neural Network Model of Short-term Horizontal Disparity Vergence Dynamics*

S. S. PATEL,† H. ÖĞMEN,†§ J. M. WHITE,‡ B. C. JIANG‡

Received 11 April 1995; in revised form 7 February 1996; in final form 2 October 1996

We present a neural network model of short-term dynamics of the human horizontal vergence system (HVS) and compare its predictions qualitatively and quantitatively with a large variety of horizontal disparity vergence data. The model consists of seven functional stages, namely: (1) computation of instantaneous disparity; (2) generation of a disparity map; (3) conversion of the disparity into a velocity signal; (4) push–pull integration of velocity to generate a position signal; (5) conversion of the position signal to motoneuron/plant activity for each eye; (6) gating of velocity overdrive signal to motoneuron/plant system; and finally (7) discharge path for position cells. Closed-loop (normal binocular viewing) symmetric step and staircase disparity vergence data were collected from three subjects and model parameters were determined to quantitatively match each subject's data. The simulated closed-loop as well as open-loop (disparity clamped viewing) symmetric step, sinusoidal, pulse, staircase, square and ramp wave responses closely resemble experimental results either recorded in our laboratory or reported in the literature. Where possible, the firing pattern of the neurons in the model have been compared to actual cellular recordings reported in the literature. The model provides insights into neural correlates underlying the dynamics of vergence eye movements. It also makes novel predictions about the human vergence system. © 1997 Elsevier Science Ltd. All rights reserved.

Disparity vergence Dynamical model Neural network Eye movements Simulations

INTRODUCTION

The human horizontal vergence system (HVS) produces the disjunctive ocular movements that are needed to maintain clear single vision when a binocular target moves in depth. These disjunctive movements result in increased convergence of the two eyes when the target moves from far to near and vice-versa. One of the most significant external inputs to the HVS is horizontal retinal disparity (Madox, 1907; Westheimer & Mitchell, 1956; Riggs & Niehl, 1960). There are other stimulus cues like blur, perceived distance, loom etc. that also affect the performance of the HVS but generally, supra-threshold luminance and chromatic properties of the stimulus do not affect it (Livingstone & Hubel, 1987). Some fundamental properties of the HVS have been established since the late 1950s, mainly by application of classical control theory. It has been shown that the HVS is primarily an integral controller with continuous feedback (Rashbass & Westheimer, 1961a). It has a typical delay of about 160 msec and possesses low-pass temporal frequency characteristics (Rashbass & Westheimer, 1961a). Furthermore, it has been shown that it operates largely in parallel (not necessarily noninteractively; Erkelens *et al.*, 1989a) with circuits controlling conjugate eye-movements (Rashbass & Westheimer, 1961b). The HVS also exhibits a "predictive" behavior in response to smooth and repetitive stimuli (Rashbass & Westheimer, 1961a).

Various studies have shown that HVS is nonlinear and adaptive (Sethi, 1986). Therefore, analytical tools from linear time-invariant system theory could not be directly applied to study the *dynamics* of the HVS. In fact, control-type dynamic models (Rashbass & Westheimer, 1961a; Krishnan & Stark, 1977; Schor, 1979; Hung *et al.*, 1986; Schor, 1992; Pobuda & Erkelens, 1993) have not been tested extensively with a wide variety of short-term‖ vergence dynamics data.

The first model by Rashbass and Westheimer (1961a) captured the most significant integral-type behavior of the HVS and clearly identified the linear relationship between disparity and vergence velocity. However, their

*This study was presented in part at the 1995 Annual Meeting of ARVO and appeared in abstract form in *Investigative Ophthalmology & Visual Science*, *36*, S457.

†Department of Electrical & Computer Engineering, University of Houston, Houston, TX 77204-4793, U.S.A.

‡College of Optometry, University of Houston, Houston, TX 77204-6052, U.S.A.

§To whom all correspondence should be addressed [*Email* ogmen@uh.edu].

‖The human vergence system exhibits adaptive changes in response to sustained stimuli of duration 10 sec and longer (Sethi, 1986). The term short-term dynamics refers to the behavior of the system without such long-term adaptation effects.

model failed to explain the open-loop sinusoidal phase responses and the open-loop ramp responses. The authors attempted to explain the discrepancies between theoretical and experimental phase responses by using higher-order disparity information. The models by Krishnan and Stark (1977) and Schor (1979, 1992) established a general principle of parallel slow and fast pathways. In addition, Schor's model includes accommodation–vergence interactions as well as long-term adaptation effects. The dual-mode model of Hung *et al*. (1986) was the first one to apply nonlinear control mechanisms to the vergence system. This model, in which vergence velocity and acceleration are used to predict position, produced convincing fits to closed-loop ramp responses. However, the model generated significantly distorted responses to closed-loop sinusoidal stimuli of frequencies >0.3 Hz. Furthermore, no open-loop responses were reported by Hung *et al*. and without an adequate description of certain (predictor and sampler) components of the model, the open-loop behavior of the model remains unknown. The recent model by Pobuda and Erkelens (1993) also uses nonlinear control mechanisms and shows improvement over the previous models in open-loop sinusoidal phase response characteristics. The model treats disparity as a spatio-temporal quantity and uses parallel disparity channels, each of which is a different first-order low-pass filter that responds only to disparity within its tuned range. The open-loop phase responses in this model result mainly from differently tuned parallel channels. In addition, the oscillations seen during closed-loop step vergence responses come from these parallel channels.

A significant behavior exhibited by all the models [except Rashbass & Westheimer (1961a)] arises due to the presence of leakiness in the modeled open-loop system. The leakiness in the vergence system implies that it returns to its resting state in the absence of a binocular target and is used to explain the decay of vergence posture in darkness. However, leakiness in the vergence system also predicts that the vergence response would reach a steady-state under open-loop step disparity conditions which means that even in presence of sustained disparity, the vergence posture would not change. Furthermore, in the linear range of operation, the steady-state vergence posture in the open-loop condition would be linearly related to the amplitude of the step disparity. This open-loop steady-state behavior is predicted by most of the models (Krishnan & Stark, 1977; Schor, 1979; Hung *et al*., 1986; Schor, 1992; Pobuda & Erkelens, 1993) except Rashbass and Westheimer's model (Rashbass & Westheimer, 1961a). In order to support the open-loop steady-state behavior exhibited by their model, Pobuda and Erkelens have presented experimental data showing vergence response reaching a steady-state before physiological eye rotation limit, even for a very small amplitude disparity step. However, these findings have not yet been replicated in other laboratories. More fundamentally, the question then arises as to why the eyes would cease to move in spite of persistent disparity when disparity is believed to be the driving signal for the vergence system. There is a significant asymmetry in convergence and divergence dynamics (Krishnan & Stark, 1977) that cannot be explained by any existing model. Further, none of the existing models is able to explain the open-loop sinusoidal phase characteristics while still maintaining the integral nature of the system.

Moreover, while each of these models was successful in explaining some characteristics of the HVS, due to the limitations of the modeling approach, physiological findings could not be directly used. Control type modeling is essentially a behavioristic approach where a "black box" representation of the system is derived from its input–output (stimulus-response) characteristics. For example, most control theory models of HVS use disparity as input and vergence eye-position as output without specifying how disparities are computed from retinal activities and how motoneurons are driven to generate the desired disjunctive movements. This tells us very little about the details of the neural circuits that control the behavior. These limitations of the "black box" modeling approach led to a complementary approach that is built around a network of neurons that aim to capture both the architecture and the function of the circuits under study by using neurophysiological, anatomical, and behavioral data. In this paper we propose a neural network model for short-term dynamics of HVS and test it extensively by comparing simulated vergence responses with a variety of experimental data.

GENERAL DESCRIPTION OF THE MODEL

The main idea behind the model is that the goal of the HVS is to provide the disjunctive oculomotor drive needed to reduce the disparity signal and thereby to move the geometric centroid of the selected target to the central part of the fovea of each eye. The general structure of the model consists of seven functional stages as shown in Fig. 1.

The model assumes the existence of retinotopic maps where localized and normalized activities are generated corresponding to the retinal locations of the target in the two eyes. The retinotopic maps, called *normalized retinotopic maps* (NRM), are separate for each eye as somewhat suggested by earlier studies (Westheimer & Mitchell, 1969). The activity in each NRM is normalized in that it does not depend on the luminance or other features of the target. It simply codes the location of the target on each retina. Such a mechanism can partially explain the movements induced by dissimilar targets in each eye (Westheimer & Mitchell, 1969), because the movement circuitry only requires an activity corresponding to the location of a target in each eye.

(1) Computation of instantaneous disparity

In this stage, the localized activities in the NRM are used to detect instantaneous disparity by a pool of neurons termed as disparity detectors. Each of these detectors receives one input from the left NRM and one

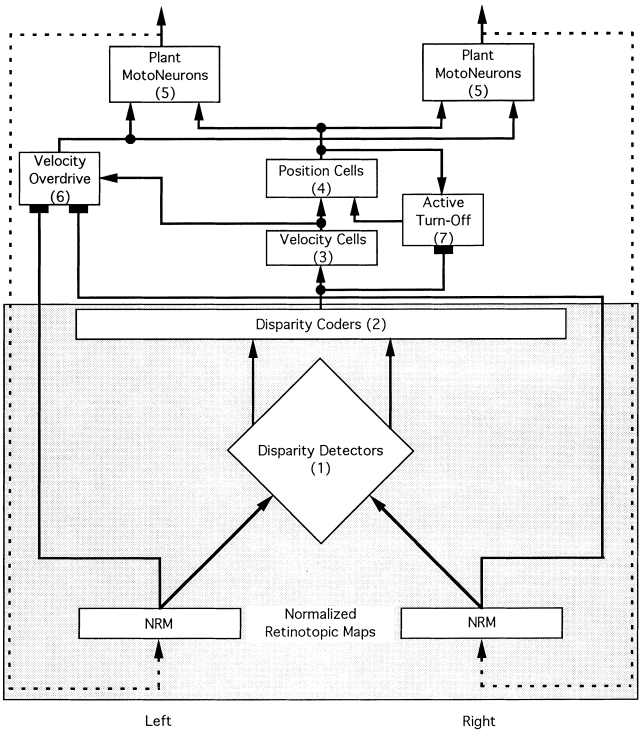

FIGURE 1. The overall block diagram of the model of the horizontal vergence system. The solid lines with arrows represent the primary signal path. The dotted lines represent the external visual feedback. The solid lines with rectangular connections show modulatory signals. For intersecting lines, a dark spot indicates a connection. The sensory stages of the model are displayed in the shaded region and the motor stages in the unshaded region. The numbers in the boxes correspond to those of the stages described in the text.

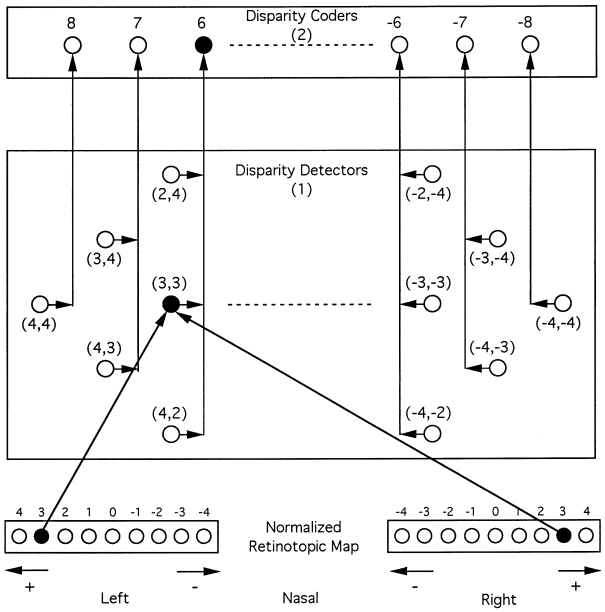

FIGURE 2. Sensory stages of the model [stages (1) and (2)]. To prevent clutter, only the connections of the active neurons, illustrated in black, are shown. In this and the following figures, a circle represents a neuron and a solid (dotted) line connecting the neurons represent excitatory (inhibitory) synapse. In each normalized retinotopic map (NKM), a binocular target activates a cell representing the geometric centroid of the target image. The activity in NRMs in turn activates a disparity detector cell in the diamond topology. Each column in this topology represents a particular disparity level. The maximum convergent disparity detector and the maximum divergent disparity detector are located at the left and the right, respectively. Cells in the diamond topology that detect the same disparity project to a single cell coding that particular disparity.

input from the right NRM and therefore has a binocular receptive field. A detector becomes active only if the corresponding retinotopic cells that feed into it are simultaneously active. Hence, when active, a detector signals a retinal disparity equal to the difference of retinotopic positions of its input neurons. By arranging these neurons into a spatial map indexed by disparity, we obtain a "diamond shaped" spatial map of disparity detectors as shown in Fig. 2. Only the cell that receives inputs from the two active cells in the NRMs is active (indicated by black in Fig. 2); all other cells in the map are inactive. For simplicity, population coding of disparity detectors is avoided. It should, however, be noted that each cell in the map represents a population effect. This is the area where the sensory drive consistent with Hering's hypothesis for the disjunctive movement is extracted (Hering, 1868). It should be noted that for purely conjugate movements, only the detectors corresponding to zero disparity are activated, thus eliminating the driving signal to the following vergence motor circuitry. For stimuli that generate combined version-vergence movements, this circuit only extracts the disjunctive component.

(2) Generation of a disparity map

A given disparity can be detected by various detectors (the vertical dimension of the diamond map). In order to generate a unique spatial coding for disparities, different cells that detect the same disparity (i.e. cells aligned in the vertical dimension of the diamond map) project to one disparity coder to generate a one-dimensional spatial map of disparity as shown in Fig. 2. Again consistent with Hering's hypothesis, the disparity code formed is independent of the conjugate component of the stimulus. Disparity tuned cells were first studied extensively in the visual cortex of the cat (Barlow *et al.*, 1967; Nikara *et al.*, 1968; Pettigrew *et al.*, 1968) to understand stereoscopic depth perception. Similar cells were also found in the monkey visual cortex (Hubel & Wiesel, 1970; Poggio & Ficher, 1977; Maunsell & Van Essen, 1983; Roy *et al.*, 1992). However, it is not clear if the same cells or a separate set of cortical or sub-cortical cells convey the disparity information needed for vergence movements.

(3) Conversion of the disparity into a velocity signal

The activity in the disparity map corresponding to a convergence (or divergence) demand is converted to a velocity signal for a convergence (or divergence) movement. The conversion is achieved by setting the synaptic strength of the connections between a neuron in the disparity map and the velocity cell to a value proportional to the magnitude of the disparity. The justification to use this mechanism for the vergence system comes from the fact that the velocity of open-loop vergence step

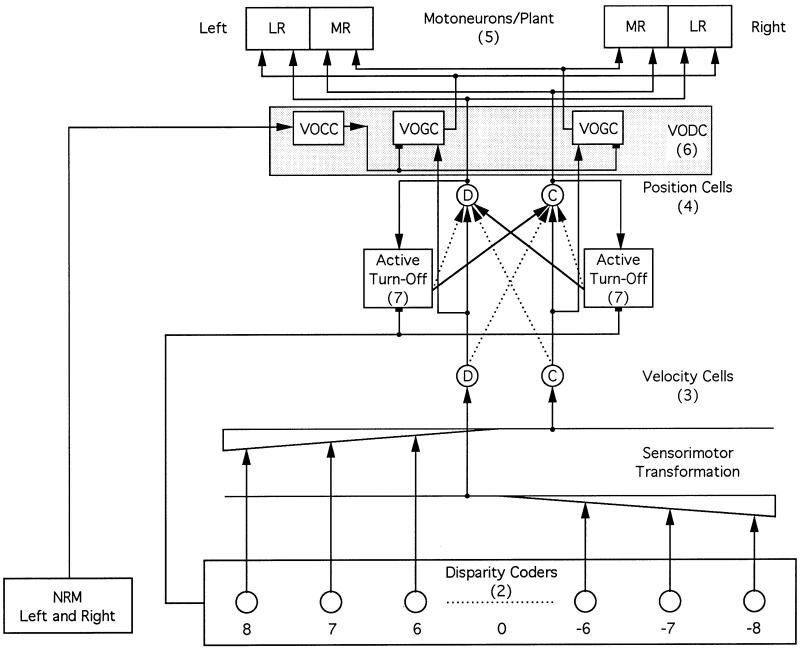

FIGURE 3. Sensory-motor transformation and the motor stages of the model [stages (3)–(7)]. In this and all following figures, for intersecting lines, a dark spot indicates a connection; a dotted line indicates an inhibitory connection. The graded connectivity between the disparity coder cells and the velocity cells is shown by the triangular section on both sides of the figure. The VODC is shown as a gray section. Velocity cells (D, divergence and C, convergence) project via the VOGC and the position cells (D, divergence and C, convergence) to lateral and medial rectus motoneurons (LR and MR). The VOGC receives control information from the VOCC. The active turn-off circuit discharges the position cells in the absence of a target. The details of VOCC, VOGC, and active turn-off circuitry are given in the following figures.

responses is linearly related to disparity (Rashbass & Westheimer, 1961a). Accordingly, as shown in Fig. 3, disparity coders with positive (negative) disparities send excitatory projections to convergence (divergence) velocity cells with weights proportional to the amount of disparity. Such vergence velocity (burst) cells have been found in the monkey midbrain (Mays *et al*., 1986).

(4) Push–pull integration of velocity to generate position signal

The velocity cells project to nonleaky position integrators in a push–pull manner. In other words, the convergence (divergence) velocity cell sends excitatory projections to a convergence (divergence) position cell and inhibitory projections to a divergence (convergence) position cell as shown in Fig. 3. Vergence position cells are also found in the monkey midbrain (Mays, 1984). For simplicity, we do not explicitly mention or use interneurons that may be needed for such a bipolar axonal connectivity. The existence of such integrators and how they are implemented in neural systems is not clear though several mechanisms have been suggested (Carpenter, 1988). From recent physiology in primates, it is also known that the abducen internuclear neurons carry an inappropriate signal during vergence movements (Gamlin *et al*., 1989). The negative effect of this pathway has to be canceled by an overdrive from another pathway. This suggests an asymmetry in the firing pattern of convergence and divergence position cells. For a symmetric convergent movement, the convergence position cell which projects to the medial rectus motoneurons, must have a larger change in firing rate from the resting rate than the divergence cell. We have ignored this mechanism in our model due to the lack of existence of a conjugate system in the model.

(5) Conversion of the position signal to motoneuron activity

The convergence and divergence position cells finally project to corresponding pools of medial and lateral rectus motoneurons. These motoneurons innervate the corresponding muscles responsible for horizontal eye movement. The convergence (divergence) position cells send excitatory projections to the medial (lateral) rectus motoneurons of both eyes as shown in Fig. 3. The motoneurons also receive inputs from corresponding velocity cells (Robinson, 1970; Keller, 1981; Gamlin & Mays, 1992). This velocity input plays a very important role in shaping the phase characteristics of sinusoidal vergence responses. For simplicity, in our model, we treat the motoneurons and plant as a single first-order system.

(6) Gating of velocity overdrive signal to motoneuron/plant system

The open-loop sinusoidal phase response of the vergence system (Rashbass & Westheimer, 1961b) differs markedly from that of a pure integral controller and suggests the involvement of a phase-lead compensation mechanism. In control theory, phase-lead compensation is used to improve the stability margin of the system and thereby to reduce the adverse effect of parasitic delays. A constant velocity input to the motoneurons has

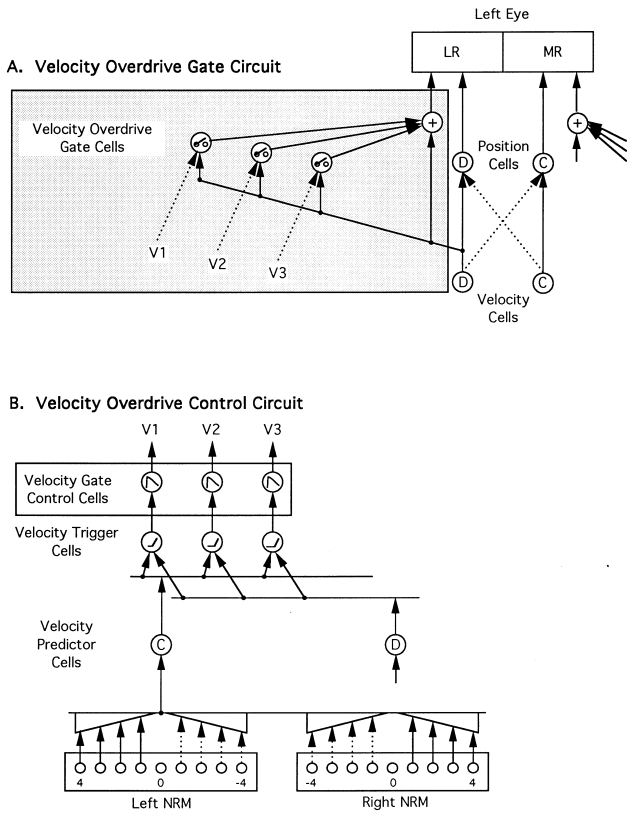

FIGURE 4. Components of the VODC. (A) The VOGC for lateral rectus. The circuit for the other muscle is identical. The velocity signal passing through the gate cells is derived from the divergence velocity cell. (B) The VOCC receives its input from both NRMs. The velocity predictor cell labeled C (D) predicts convergence (divergence) velocity. The convergence velocity predictor cell has a graded input connectivity (shown by triangular sections) from the NRMs. The divergence velocity predictor cell has the same graded connectivity from NRMs but with a negative sign applied to each input.

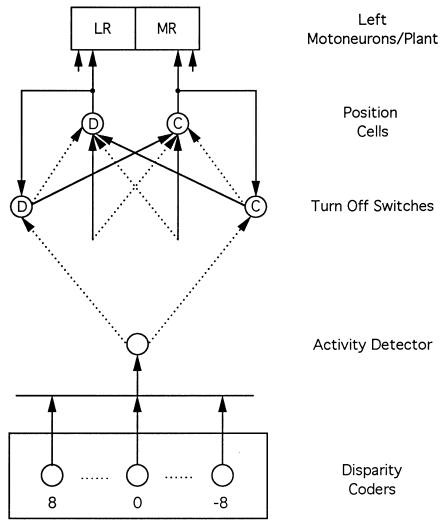

FIGURE 5. Active turn-off circuit. The activity detectors signal the presence of a binocular visual target. The turn-off switches act on the position cells in a push–pull manner. The rest of the circuit is not shown and is indicated by lines without originating circles.

been previously proposed to overcome the viscous impedance in the muscles and orbit (Robinson, 1981). We have introduced a phase-lead to our model by a velocity overdrive circuit (VODC) with discrete parallel channels, each gated by a preset velocity threshold as shown in Fig. 4. The parallel channels generate a variable velocity input for the motoneurons as a function of velocity, in particular a high input for low velocities and a low input for high velocities. For simplicity we used only three parallel channels in our simulations. However, in the vergence system there would be a large number of parallel channels providing a finer resolution, thus resulting in a smoother velocity control mechanism.

The VODC consists of one velocity overdrive control circuit (VOCC) and two velocity overdrive gate circuits (VOGC), one for each muscle. In order to provide an adaptive velocity control, a fast estimate of velocity is computed by the VOCC. This predicted velocity is used to gate the appropriate velocity channels of the VOGC. As shown in Fig. 4(b), the gate switching signals (V1, V2, V3) are derived from velocity predictor cells. The convergence velocity predictor cell receives input via a graded excitatory (inhibitory) connectivity directly from the temporal (nasal) side of the NRM of each eye. The connectivity for the divergence velocity predictor cell is complementary (negative) of that of the convergence cell. Each velocity trigger cell in VOCC senses the velocity level and fires if the velocity level exceeds the cell's threshold (different for each cell). In our recruitment scheme, threshold increases from V1 to V3. Thus at the smallest velocity, V1 would be active, at some intermediate velocity V1 and V2 would be active and at velocity above a certain level, all of them would be active. The velocity trigger cells then activate the velocity gate control cells which have a fast on-time and a very slow off-time.

The velocity gate control cells in VOCC strongly inhibit the velocity overdrive gate cells (VOG) in VOGC and keep them inactive for a significant period of time (*ca* 1 sec). As shown in Fig. 4(a), the signal from the vergence velocity cell is simultaneously sent to all VOGs. Hence if all gate cells are active, the signal sent to the plant via the summing cell is maximal. During step movements, all gate cells are off, hence reducing the velocity drive that may have otherwise caused oscillations. For low and medium frequency sinusoidal stimuli (0.05–0.4 Hz), all or some of these cells are active, thus providing a velocity overdrive and causing a phase-lead. It should be noted that the velocity predictor cells, which are also active during monocular viewing, only provide a gate control signal hence they have no effect if a disjunctive stimulus is absent. There is some experimental evidence supporting the hypothesis that a velocity driven signal contributes to the control of vergence eye-movements in primates and that the contribution of this velocity drive is different during sinusoidal and step stimulation of the vergence system (Gamlin & Mays, 1992).

(7) Discharge path for position cells

The nonleaky nature of position integrators implies

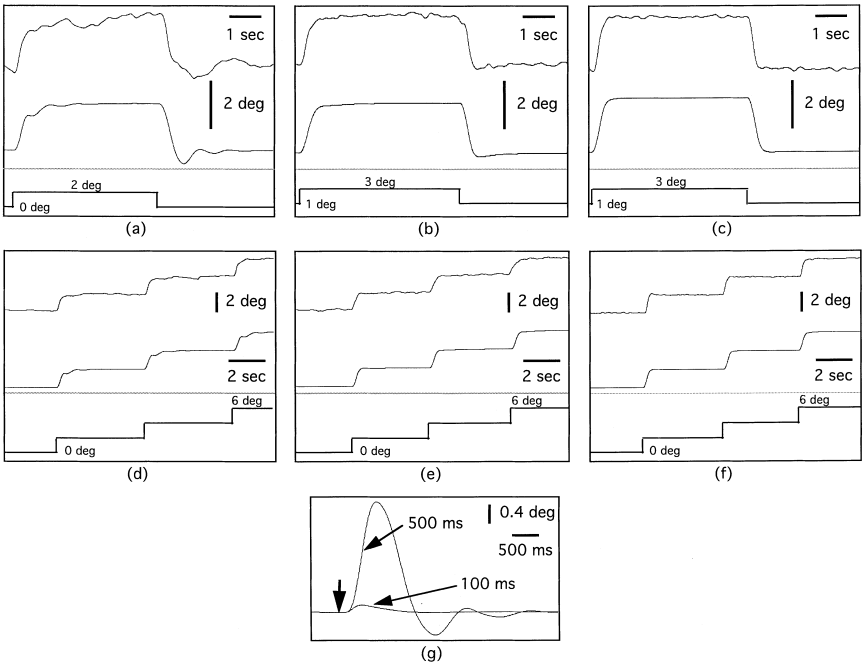

FIGURE 6. Closed-loop step, staircase and short-pulse responses. For this and all the following figures: (i) deviations in vergence position traces towards the top indicate increased convergence. (ii) An arrow without a label indicates stimulus onset or offset. (a)–(c) Experimental and simulated closed-loop 2-deg step response for subjects LFH, NYN, and VTA, respectively. The step duration was 5 sec. (d)–(f) Experimental and simulated closed-loop staircase response for subjects LFH, NYN, and VTA, respectively. Each step was 2 deg and the step duration was 5 sec. (g) Simulated closed-loop short-pulse responses to 100 and 500 msec pulse stimulus. The pulse stimulus amplitude was 2 deg.

that, in the absence of an input, the eyes maintain their position. An active turn-off circuit is introduced to move the eyes to their "resting positions" in the absence of activity in the disparity coders (see Fig. 5). This mechanism provides independent control of dark-vergence dynamics from stimulus-driven dynamics.

METHODS

Closed-loop vergence responses to step, staircase and sinusoidal stimuli were measured in human subjects, to compare with similar data in the literature and the simulated responses of our model. Three naïve volunteers (LFH, NYN, and VTA) with normal binocular vision participated in the experiments. We developed a Macintosh-based system to concurrently provide vergence stimuli and record binocular eye movements. The vergence stimuli were rectangular targets (9 deg in height and 0.35 deg in width) presented haploscopically, using two computer monitors viewed separately by each eye from mirrors at 45 deg from the line of sight. The white rectangular targets on black backgrounds were the only targets visible during the experiments. For step stimuli, the symmetrical vergence demand alternated between 0 deg and several different levels of convergence (up to 4 deg). All step stimuli were presented for a maximum of 5 sec to minimize adaptation effects. For sinusoidal stimuli, the symmetrical vergence demand varied 2 deg peak-to-peak around 2 deg of convergence, at six frequencies between 0.05 and 3.2 Hz. The rectangular targets also acted as accommodative stimuli, fixed at *ca* 0 diopters (achieved by placing convex lenses in the optical path of each eye).

Vergence eye movements were recorded using two dual Purkinje-image eye trackers (Crane & Steele, 1978). The eye trackers generate a voltage signal proportional to horizontal eye position which was digitized, sampled at 60 Hz and stored by the computer. Since the gain of the disparity vergence system drops about 40 dB at 1.5 Hz (Zuber & Stark, 1968; Pobuda & Erkelens, 1993), a 60 Hz sampling rate is more than adequate. A signal representing the position of each target on the monitor was generated on D/A converters and re-sampled and stored along with the eye position signals. Before collecting the vergence data, a monocular calibration procedure was run on each eye. During the calibration procedure, the target stepped horizontally from 0 to 4 deg in steps of 1 deg. After calibrating each eye's position data independently, the vergence response was computed by subtracting the position data of the two eyes. All data were analyzed using the signal processing package AcqKnowledge (Biopac Systems Inc.). The step and staircase responses were averages of two trials.

Simulation methods are given in Appendix B.

RESULTS

All subjects exhibited qualitatively similar results as reported in the literature (Riggs & Niehl, 1960; Rashbass & Westheimer, 1961a; Zuber & Stark, 1968; Krishnan &

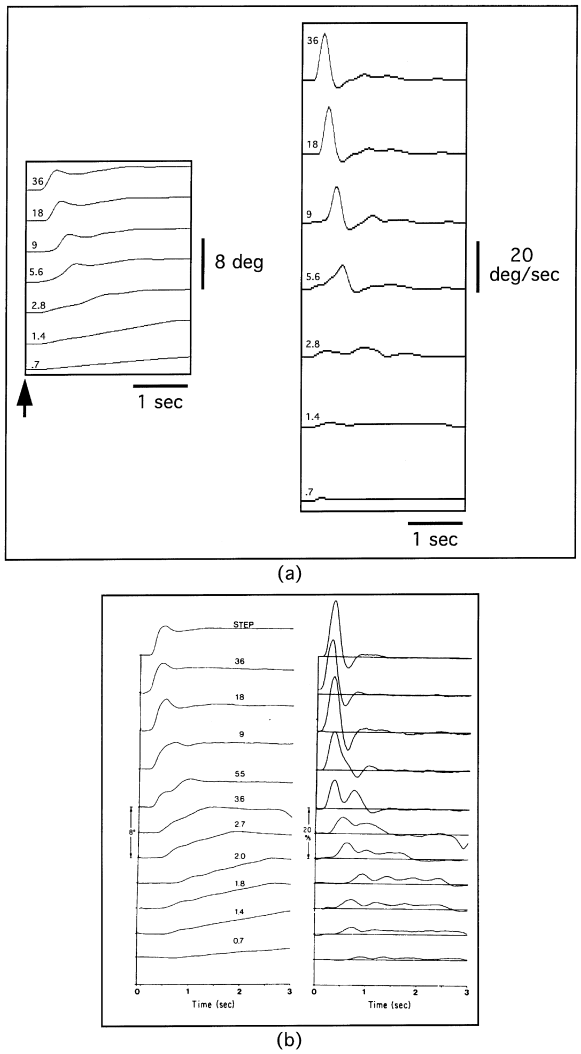

FIGURE 7. Closed-loop ramp responses. (a) Simulated closed-loop responses to convergent ramps from 0.7 to 36 deg/sec are shown in the left panel. The peak amplitude was 4 deg. The computed velocity traces for the responses in the left panel are shown in the right panel. (b) Experimental recordings obtained by Semmlow *et al*. (1986). The left column shows the position traces while the right one shows the corresponding calculated velocity traces. Reprinted with permission from the journal *Investigative Ophthalmology & Visual Science.*

Stark, 1977; Hung *et al*., 1986; Erkelens *et al*., 1989b; Pobuda & Erkelens, 1993) in all experiments. Step and staircase responses were obtained for all the subjects while sinusoidal responses were obtained only for one subject (LFH). Model parameters were adjusted so that model responses approximated the step and staircase data for all the subjects, and for one subject (LFH) a single parameter set was obtained to approximate the step, staircase, and sinusoidal data.

Closed-loop responses

Our closed-loop step responses show the typical characteristics reported in the literature (Rashbass & Westheimer, 1961a): a 160 msec delay, a fast "open-loop" initial response followed by a slow completion (Semmlow *et al*., 1993) with small oscillations (Rashbass & Westheimer, 1961a) as shown in Fig. 6(a–c). Our closed-loop staircase responses shown in Fig. 6(d–f) indicate the typical motor linearity associated with vergence movements.

The experimental and simulated closed-loop step responses [Fig. 6(a–c)] are qualitatively very similar. Quantitatively, for subject LFH, the overshoot observed during step divergence [downward deflection in Fig. 6(a)]

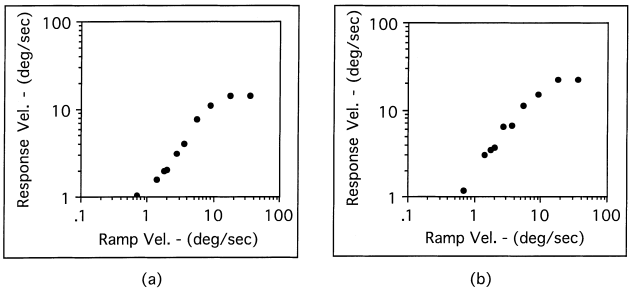

FIGURE 8. Ramp stimulus-response curves. (a) Simulated stimulus-response curve for various ramp velocities from 0.7 to 36 deg/sec. The value used for this plot is the maximum velocity. Notice the saturation in the curve. (b) Peak ramp response velocity vs stimulus velocity obtained by Semmlow *et al*. (1986). Reprinted with permission from the journal *Investigative Ophthalmology & Visual Science.*

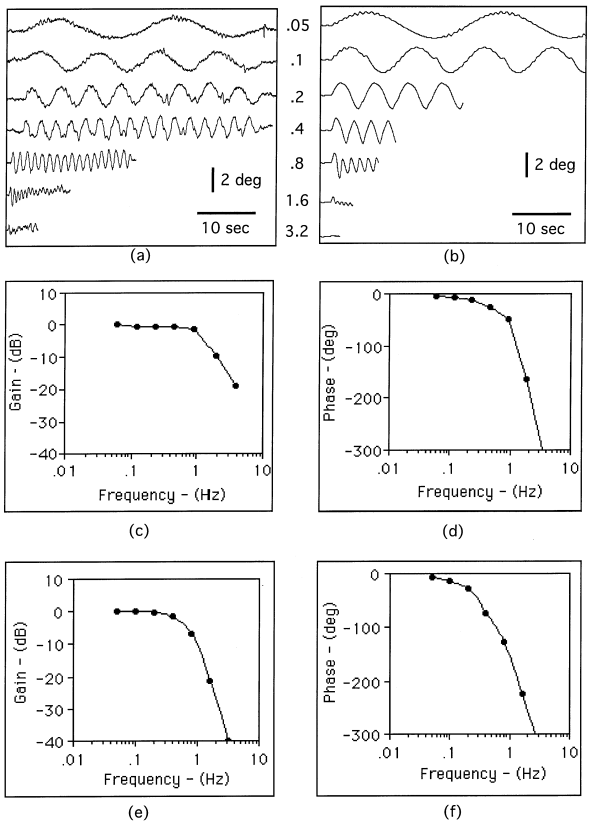

FIGURE 9. Closed-loop sinusoidal responses. (a) Experimental closed-loop sinusoidal responses for frequencies from 0.05 to 3.2 Hz and peak to peak amplitude of 2 deg. The sinusoidal stimulus was applied after an initial convergent step of 2 deg. (b) Simulated closed-loop sinusoidal responses for frequencies from 0.05 to 3.2 Hz and peak to peak amplitude of 2 deg. The sinusoidal stimulus was applied after an initial convergent step of 2 deg. (c) and (d) are experimental closed-loop sinusoidal gain and phase plots, respectively. (e) and (f) are simulated closed-loop sinusoidal gain and phase plots, respectively.

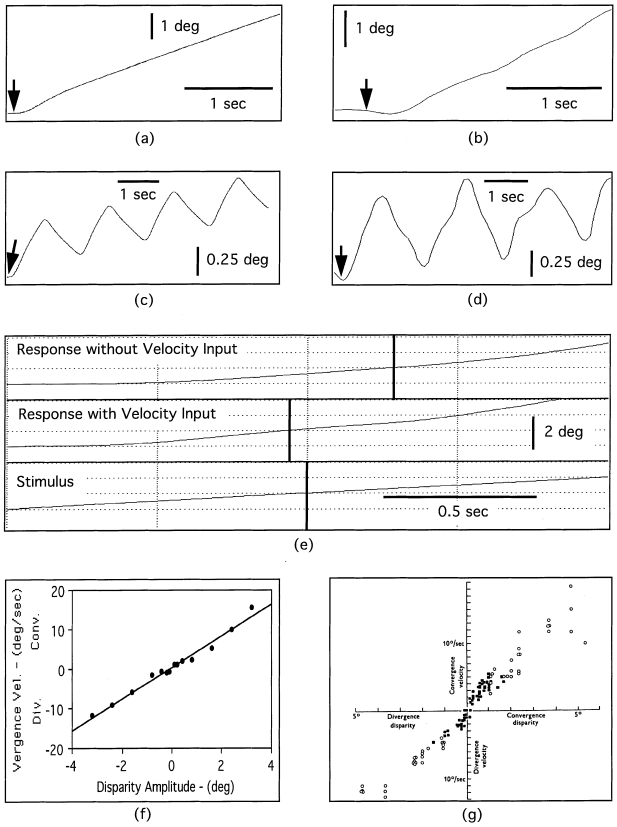

FIGURE 10. Open-loop step, ramp and square-wave responses. (a) Simulated open-loop step response to a disparity step of 0.4 deg. (b) Open-loop response to a disparity step recorded by Rashbass and Westheimer (1961b). (c) Simulated open-loop response to a square wave of 0.6 Hz with a peak to peak amplitude of 0.4 deg. (d) Open-loop square wave response recorded by Rashbass and Westheimer (1961b). (e) Simulated open-loop response to a ramp of 1 deg/sec without velocity input is shown in the top panel and with velocity input is shown in middle panel. The stimulus is shown in bottom panel. The thick vertical line in each panel indicates the instant of zero disparity crossing. To the left (right) of the thick line, the disparity is negative (positive). (f) Simulated open-loop convergence velocity vs step disparity amplitude from −3.5 up to 3.5 deg. (g) Experimental data establishing the relationship between disparity amplitude and vergence velocity from Rashbass and Westheimer (1961a). The open circles represent data points obtained from the initial phase (<160 msec) of the closed-loop step responses while the dark circles are true open-loop data points. Figures from Rashbass and Westheimer (1961a,b) published with permission from the Physiological Society.

is somewhat different. These differences are not in the initial fast part of the response but in the final settling part and are dictated by the limited resolution of the NRM in our simulations. The subjects NYN and VTA showed less pronounced oscillations [Fig. 6(b–c)] during the completion phase and the model fits for them were obtained by reducing the velocity input to the motoneurons/plant system (see parameters in Appendix B). Subject VTA showed symmetric convergence and divergence characteristics [Fig. 6(c)] that were modeled by symmetric sensorimotor transformation (see parameters in Appendix B).

The experimental and simulated closed-loop staircase responses [Fig. 6(d–f)] are also qualitatively very similar. Subject VTA [Fig. 6(f)] showed superior linearity characteristics over the other subjects hence its staircase data were modeled by a smaller synaptic gain at the position cells and a proportionally larger gain at the motoneurons/plant (see parameters in Appendix B). The simulated pulse responses shown in Fig. 6(g) exhibit general characteristics of the HVS reported in the literature (Rashbass & Westheimer, 1961a; Zuber & Stark, 1968). The smallest pulse-width that generated a simulated response was 100 msec which can be attributed to the rise-times of the cells in the NRM. If enough time is not allowed for these cells to rise above the threshold of the disparity detectors, no response can be generated. This mechanism generates response delays larger than those predicted by axonal and synaptic delays. Since a major portion (100 msec) of the delay was exhibited at the stage between the NRM and the disparity detectors, the delay mechanism is not a pure delay as previously proposed (Rashbass & Westheimer, 1961a). However, if this delay is distributed such that a maximum delay of 20 msec is introduced at each processing stage, then the model will respond to a minimum pulse of 20 msec while maintaining the large total delay.

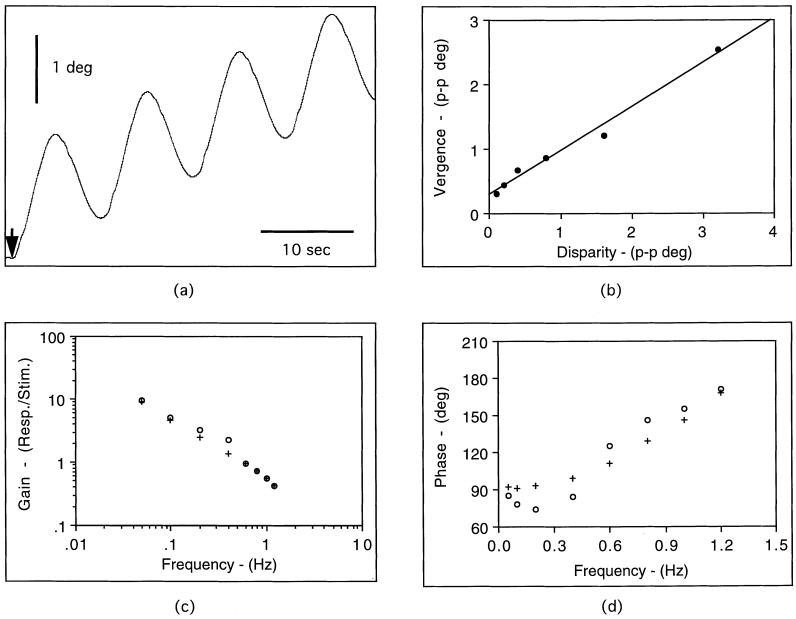

FIGURE 11. Open-loop sinusoidal responses. (a) Simulated open-loop sinusoidal response at 0.1 Hz and peak to peak amplitude of 0.4 deg. The sinusoidal stimulus was applied after an initial convergent step of 2 deg. (b) Simulated stimulus–response curve for various sinusoidal amplitudes from 0.1 to 3.2 deg at a frequency of 0.5 Hz. (c) Simulated open-loop sinusoidal gain response, the peak to peak stimulus amplitude was 0.4 deg. The circles are with velocity overdrive and crosses are without it. (d) The open-loop phase response for the same simulations. Again the circles are with velocity overdrive and crosses are without it.

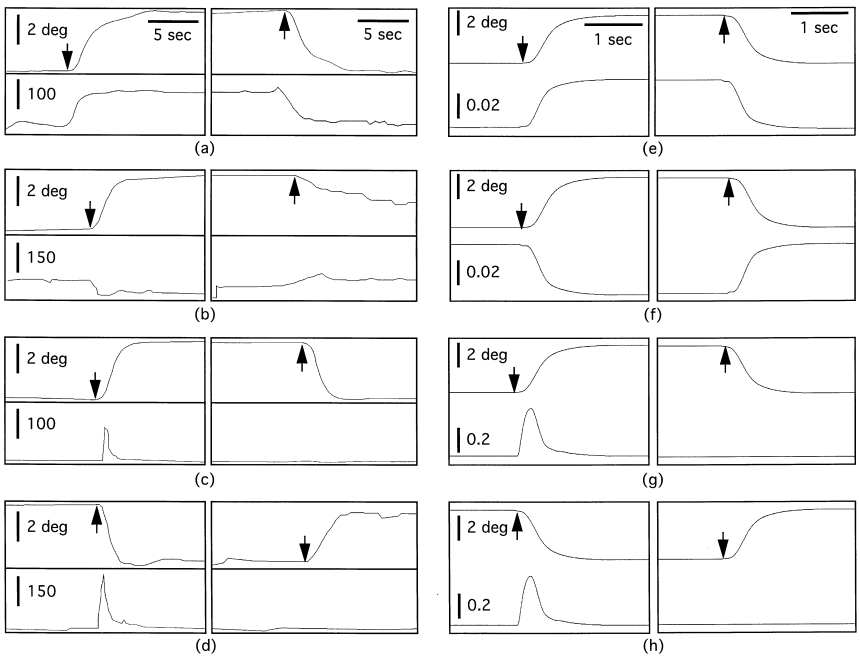

FIGURE 12. Neurophysiology and correlated model cells. In all the panels, the top trace is vergence movement and the bottom trace is the firing pattern in spikes per second. For this and all the following figures, an upward deviation in traces showing firing pattern indicates increased firing rate. The vergence step was 4 deg from a straight ahead 0 deg position for all movements, experimental and simulated. (a) Firing rate profile of a convergence cell in a monkey during vergence movements as recorded by Mays (1984). The left column shows behavior during convergence and the right one shows the behavior of the same cell during divergence. (b) Similar profile as in (a) for a divergence cell recorded by Mays (1984). (c) Firing rate profile of a convergence burst cell in a monkey during vergence movements as recorded by Mays *et al*. (1986). The left column shows behavior during convergence and the right one shows the behavior of same cell during divergence. (d) Similar profile as in (c) for a divergence burst cell recorded by Mays *et al.* (1986). (e) The firing pattern of a model convergence position cell during vergence movements. (f) The firing pattern of a model divergence position cell during vergence movements. (g) The firing pattern of a model convergence velocity cell during vergence movements. (h) The firing pattern of model divergence velocity cells during vergence movements. Figs 12(a)–(d) have been reprinted with permission from the American Physiological Society.

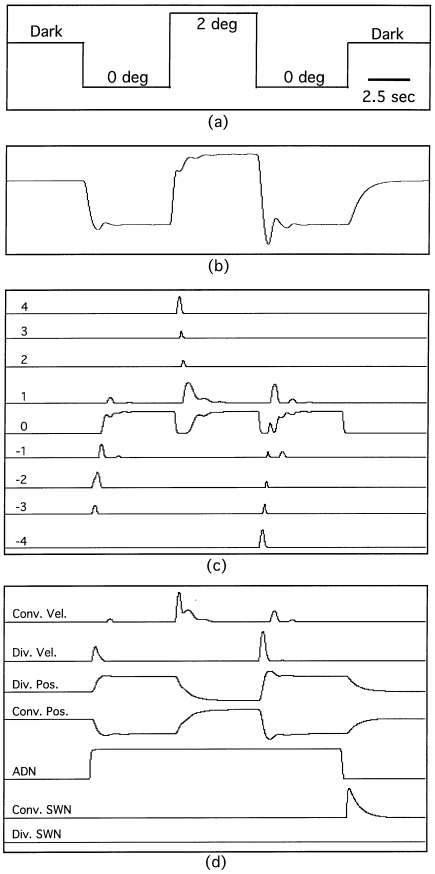

FIGURE 13. Firing patterns of model cells. (a) Typical stimulus paradigm. (b) Vergence response to the paradigm in (a). (c) Typical firing pattern in the disparity coder map under conditions of darkness, 0 deg vergence and 2 deg convergence conditions. The numbers in the panel indicate the disparity coder position in the map of coders. (d) Typical firing pattern in the position, velocity and turn-off circuitry cells under previously mentioned conditions and convention. ADN is the activity detector cell and SWNs are switch cells in the active turn-off circuit.

The simulated closed-loop ramp responses and their corresponding velocities are shown in Fig. 7(a). For comparison purposes data taken from Semmlow *et al.* (1986) are shown in Fig. 7(b). For low ramp velocities, smooth ramp responses and constant velocities are observed in both simulated and experimental data. For higher velocities, the response velocity is no longer constant but exhibits oscillations which correspond to step-like behavior in the position traces. Our model suggests that the oscillations in the response velocity are caused by the contribution of the velocity input (VODC) to motoneurons, in that the model in pure position control mode does not exhibit such oscillations. Furthermore, in both simulated and experimental data, the peak response velocity saturates as shown in Fig. 8. We believe that quantitative differences, such as the saturation level, come from inter-subject variability.

The experimental and simulated closed-loop sinusoidal responses are shown in Fig. 9(a) and (b). Micro-oscillations are seen in experimental as well as simulated data for lower frequencies. In the simulations, the micro-oscillations are due to the high velocity gain provided by the VODC. As frequencies become higher, this overdrive mechanism is turned off and the HVS returns to a dominant position control mode, thus making the responses smoother. The corresponding experimental gain and phase plots are shown in Fig. 9(c) and (d). They closely resemble the simulated gain and phase plots shown in Fig. 9(e) and (f). The simulated dark-vergence dynamics (not shown) exhibited the decay characteristics similar to the experimental data (not shown). The dark-vergence dynamics are achieved by the active turn-off circuits employed in the model.

Open-loop responses

Because the continuous feedback compensation is eliminated, open-loop responses reveal more directly the characteristics of a system and thus offer a critical test to models. The open-loop simulation results presented here were obtained by using the same parameters that were used for closed-loop simulations. As shown in Fig. 10, the simulated open-loop step response exhibits an integral nature very similar to the experimental recording (Rashbass & Westheimer, 1961a) shown in Fig. 10(b). The simulated open-loop square-wave response is a drifting triangular waveform as shown in Fig. 10(c), similar to the experimental recording (Rashbass & Westheimer, 1961a) shown in Fig. 10(d). Our model suggests that this drift in open-loop response originates from the lack of feedback and the asymmetry between convergence and divergence characteristics. The simulated open-loop ramp response is shown in Fig. 10(e). The use of velocity information by the motoneurons/plant system in our model clarifies why the open-loop ramp response crosses the zero disparity point *before* the stimulus, an observation made by Rashbass and Westheimer (1961a). This is illustrated through simulations of the model with and without velocity control as shown in Fig. 10(e). As seen in experimental data taken from Rashbass and Westheimer (1961a) [Fig. 10(g)], under open-loop conditions the model exhibits a nearly linear relationship between vergence velocity and disparity amplitude [Fig. 10(f)]. The scales of Fig. 10(f) and Fig. 10(g) are different because of a larger range requirement for the velocity axis for modeled data.

The simulated open-loop sinusoidal response is a drifting sinusoid as shown in Fig. 11(a). Figure 11(b) shows peak-to-peak vergence amplitude as a function of peak-to-peak stimulus disparity. Corresponding experimental data (Rashbass & Westheimer, 1961a) (not shown), are confined to a small range of disparities. There is some similarity between our model behavior and the experimental data within this range. However, our model shows a linearity for disparities at least up to 3.5 deg at the stimulation frequency of 0.5 Hz. Rashbass and Westheimer interpreted their results as a saturation beyond 1 deg of disparity. They did not however specify their stimulus frequency. The simulated gain and phase responses are shown in Fig. 11(c) and (d). In each plot, the crosses (circles) represent the response of the model

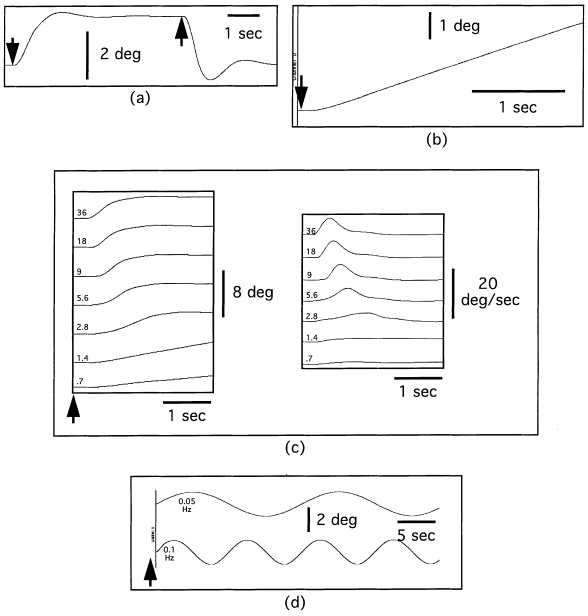

FIGURE 14. Simulated vergence responses with zero velocity input to the motoneurons/plant. (a) Closed-loop 2-deg step response for subject LFH. The step duration was 5 sec. (b) Open-loop step response to a disparity step of 0.4 deg. (c) Simulated closed-loop responses to convergent ramps from 0.7 to 36 deg/sec are shown in the left panel. The peak amplitude was 4 deg. The computed velocity traces for the responses in the left panel are shown in the right panel. (d) Closed-loop sinusoidal responses to a 2 deg p–p stimulus at 0.05 and 0.1 Hz.

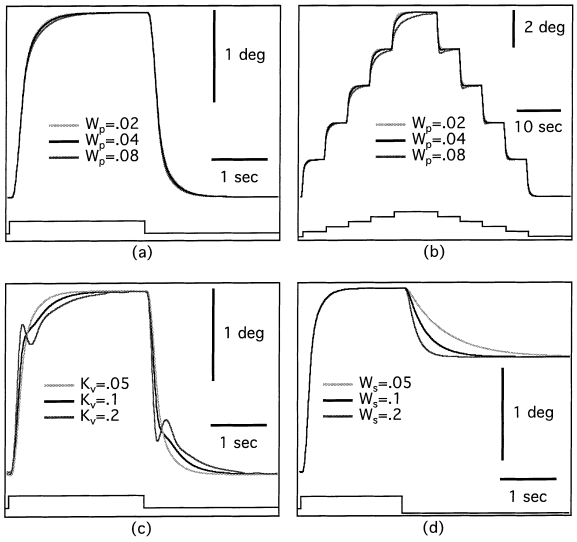

FIGURE 15. Effect of parametric variations on simulated vergence responses. The parameters specified here are described in Appendix B. (a) Closed-loop 2-deg step response under various synaptic gains at the position cells. The synaptic weights between the velocity and position cells were set as follows:

$$w_{V\Uparrow,P\Uparrow} = w_{V\Downarrow,P\Downarrow} = W_p$$

and

$$w_{V\Uparrow,P\Downarrow} = W_{V\Downarrow,P\Uparrow} = -w_p.$$

Correspondingly, the position gain between the position cells and the motoneurons/plant was set as follows:

$$K^L_{P\Uparrow} = K^L_{P\Downarrow} = K^R_{P\Uparrow} = K^R_{P\Downarrow} = 0.04/W_p.$$

The velocity gain at the motoneurons/plant was set as follows:

$$K^L_{V\Uparrow} = K^L_{V\Downarrow} = K^R_{V\Uparrow} = K^R_{V\Downarrow} = 0.001/W_p.$$

(b) Closed-loop staircase responses with the same parameters that were used for the step responses in (a). Each step was 2 deg. (c) Closed-loop 2-deg step responses under various velocity gains at the motoneurons/plant system. The velocity gain at the motoneurons/plant was set as follows:

$$K^L_{V\Uparrow} = K^L_{V\Downarrow} = K^R_{V\Uparrow} = K^R_{V\Downarrow} = K_v.$$

The position gain between position cells and both the plants was constant and set to 2. (d) Dark vergence decay under various synaptic gains between the turn-off switches and the corresponding position cells. The synaptic weights were set as follows:

$$w_{S\Downarrow,P\Uparrow} = W_{S\Uparrow,P\Downarrow} = W_s$$

and

$$w_{S\Uparrow,P\Uparrow} = w_{S\Downarrow,P\Downarrow} = -W_s.$$

without (with) the VODC. The velocity overdrive has a very small effect on the gain response but has a significant phase reducing (<90 deg) effect at lower frequencies. These results are in qualitative agreement with the experimental data (not shown) reported by Rashbass and Westheimer (1961a).

Firing patterns of model cells

A comparison between firing patterns of model cells with actual vergence velocity and position cells recorded from monkeys (Mays, 1984; Mays *et al*., 1986) is shown in Fig. 12. Notice that the vergence step responses in monkeys [Fig. 12(a–d)] are significantly slower than similar responses in humans [Fig. 12(e–h)]. The position cells in monkeys fire at least 10–30 msec before the eyes move indicating a small delay during motoneuron recruitment or plant movement. In our simulations, the entire motoneuron and plant are approximated by a first-order system, hence such a delay is not seen in the model cell patterns. The neural responses shown in Fig. 12(a–d) exhibit symmetric convergence–divergence behavior. Therefore, for comparison purposes, we used symmetric parameters. The neural firing patterns closely resemble simulated firing patterns for both position and velocity cells.

Figure 13 shows firing patterns of various model cells during dark and step stimuli conditions. The patterns for retinotopic maps and disparity detectors are not shown due to the large number of neurons involved in these pools. The stimulation paradigm and the corresponding vergence response are shown in Fig. 13(a and b), respectively. Figure 13(c), shows the firing pattern of the disparity coders between −2 and 2 deg. The pattern of activity in the network of disparity coders show a traveling wave from large disparities toward zero disparity. In Fig. 13(d), we show the firing patterns of position and velocity cells, and the cells in the active turn-off circuitry.

Other characteristics

Since we do not model accommodation–vergence interactions, it is appropriate to currently leave out

open-loop vergence conditions caused by monocular viewing. After a vergence effort, the actual position of the blocked eye is believed to be determined mainly by the accommodative posture of the viewing eye. Recent open-loop step response data have indicated a ramp-step like behavior (Semmlow *et al*., 1994). It should be noted that data from other researchers (Pobuda & Erkelens, 1993) do not show this behavior. There is evidence of the open-loop step response reaching a steady state before reaching the physiological limits (Pobuda & Erkelens, 1993). Our model currently cannot explain these data. The motor threshold observed in vergence movements (Riggs & Niehl, 1960; Duwaer & van Den Brink, 1981) can be implemented by increasing the threshold of the detectors in the NRM or in the map of disparity coders. Due to the low resolution of the NRM in our simulations, we have ignored the motor threshold for reasons of simplicity.

DISCUSSION AND CONCLUSION

Analysis of the model

To understand the effects of velocity drive to the plant Fig. 14 shows the simulated responses obtained by blocking the velocity input to the plant. The blocking includes the constant as well as the overdrive component of the vergence velocity while keeping all other parameters (LFH) the same. The step response in Fig. 14(a) does not show the pronounced oscillations near the steady-state amplitude of the response. This supports our earlier claim that these oscillations occur as a result of the velocity (fixed and variable) input to the plant. Furthermore, as seen in Fig. 14(b), the open-loop integral characteristics do not show a significant difference when compared to the response in Fig. 10(a). As seen in Fig. 14(c), the ramp-step like behavior observed at medium ramp velocities (1.4–5.6 deg/sec) is also eliminated when the velocity drive to the plant is removed. Finally, as shown in Fig. 14(d), the micro-oscillations at lower sinusoidal frequencies are also eliminated when the velocity drive, in particular the variable drive, is blocked. All this evidence put together suggests a strong possibility of a velocity drive to the plant. Furthermore, such a drive must be variable in nature.

Further analysis of the model reveals the significance of certain model parameters in controlling the linearity, the dark decay and the oscillatory characteristics of the vergence system. Figure 15(a) shows that similar step responses are obtained by keeping the product of synaptic gain at the position cells and the position gain at the motoneurons/plant system constant. Also kept constant is the ratio of the position gain to the velocity gain at the motoneurons/plant system. However, under the same conditions as above, Fig. 15(b) clearly indicates the increase in motor nonlinearity with increase in synaptic gain at the position cell. These simulations suggest that a smaller membrane potential operating range of the position cells followed by a larger linear amplification would result in linearity over a larger vergence range.

For the response shown in Fig. 15(c), all the model parameters are held constant while the velocity gain at the motoneurons/plant system is varied. As the velocity gain is increased, oscillations near the completion phase of the responses also increase. These responses provide further evidence of the role of the velocity signal in generating these oscillations. It should, however, be noted that the delay in the system also plays a role in generation of these oscillations, particularly when the velocity gain is high.

The dark vergence decay characteristics are controlled by the synaptic weights between the position cells and the corresponding turn-off switch cells. Since a push–pull negative feedback loop is formed when the switch cells are activated, the decay rate would be directly related to the synaptic weight described above. Figure 15(d) shows that the decay rate is larger for a larger synaptic weight while keeping all other parameters constant.

Model predictions

Dark vergence dynamics and the active turn-off circuit. In our model, the position integrators are nonleaky. Hence, the decay characteristics in the absence of target are independently determined by an active turn-off circuit. The model thus predicts the presence of such a circuit for the human vergence system. One may expect to find cells closer to the mid-brain that exhibit a behavior similar to the switch cells (SWN) in the active turn-off circuit of the model. There should be cells that indicate the presence or absence of a binocular target and they could be closer to the areas that perform sensory-motor transformations. Schor's (1992) and Krishnan's and Stark's models (1977) predict an exponential decay under conditions of darkness. The dark vergence decay dynamics obtained from our model are indistinguishable from the corresponding exponentials. Observation of dark vergence dynamics thus cannot uncover the underlying mechanism of decay. The model, however, predicts that such a mechanism is necessary if the position integrators are nonleaky, and if the integrators are nonleaky, then the vergence output would not reach a steady-state prior to reaching a fixed physiological (maybe plant) limit when the input disparity is held constant. In other words, outside the motor threshold range, the vergence steady-state level is independent of the magnitude of the clamped disparity. Thus an open-loop experiment where disparity is held constant at two small amplitudes (0.25 and 0.5 deg) can indirectly provide evidence for an active turn-off mechanism. If the vergence system is nonleaky, then the responses to both the disparity steps would reach the same steady-state level.

Motor nonlinearity. The motor linearity aspect of the vergence system can be uncovered by a staircase stimulation paradigm. In an equi-step paradigm, the sensory inputs in general come from the same spatial locations on the retina. The initial motor position is, however, different for each subsequent step. Perfect motor linearity is exhibited if the dynamical response of all steps is identical. As an example, a paradigm where a

12 deg vergence staircase is formed by six steps of 2 deg each, presented for a maximum duration of 5 sec. The peak velocity of each 2 deg step response can be used to compare the dynamics of each step. In the case of perfect linearity as indicated by most current models (Schor, 1992; Krishnan & Stark, 1977; Pobuda & Erkelens, 1993), the peak velocity will be equal for all steps. However, our model predicts that the peak velocity of convergence (divergence) steps could decrease (increase) as the initial motor position becomes more converged. The word "could" is used because the change in peak velocity of convergence or divergence depends on the membrane potential operating point and the operating range of position cells. This is a direct consequence of the nonlinear position integrators and the push–pull integration scheme used in our model. However, for a small range (4–6 deg) of vergence positions, the peak velocity could remain constant; i.e. a linear range of operation for the position cells. The linear range may vary from individual to individual and is related to the input synaptic gain and the firing function gain that enclose the membrane potential nonlinearity, in other words, the operating point of the position integrators. The model also predicts that the step response completion time (analogous to the time-constant) could also increase with increased convergence. This is also as a result of the nonlinear behavior of the position cells.

Steady-state vergence errors. Previous models have associated vergence errors with leakiness in the open-loop vergence system (Schor, 1979, 1980). Since our model uses disparity as a spatio-temporal quantity, under steady-state it remains a spatial quantity. Further, due to the use of nonleaky position integrators, the vergence errors in our model are disociated from open-loop leakiness. Analogous to the point spread function of an optical system, there exists a disparity spread function which may be defined as the output of the sensory system when stimulated binocularly by a point target. Hence the equilibrium in the vergence system is achieved by actively balancing the convergence and divergence activities generated by various disparity spread functions. This concept of equilibrium leads to a novel hypothesis about the origin of steady-state vergence errors. Our model predicts that the steady-state vergence error arises as a result of asymmetry between the convergence and divergence sub-systems. The open-loop gain of the vergence system is very small compared to those used in linear models (Hung & Semmlow, 1980) to explain the small steady-state vergence error (Rashbass & Westheimer, 1961a). Our explanation of the vergence error does not require a large open-loop gain in the vergence system. The staircase paradigm can be used to obtain the correlation between the steady-state errors and the peak velocity during convergence and divergence at each vergence posture.

Relation to other models

Our model shares several properties with neural network models proposed for other types of eye movements, namely pursuit (Eckmiller, 1981) and saccades (Grossberg & Kuperstein, 1989). While these models use similar building blocks, they differ in their architectures due to the different properties they synthesize. Since our model is designed to generate *disjunctive* eye movements, both our input stage and the final mapping to motoneurons are different. Our input stage consists of a specialized architecture that computes disparity. Various models for disparity computations have been proposed for depth perception (Dev, 1975; Marr & Poggio, 1976) but their role in eye-movements was not clearly indicated. While these models compute steady-state disparity, in our model we compute instantaneous disparity to generate delayed continuous feedback. While the saccadic models use a local feedback (nonvisual) type of control, our model is designed to use continuous visual feedback. Our model also differs in the specialized circuits contributing to motor control (e.g. velocity overdrive and discharge circuits).

Summary

Our model uses an adaptive nonlinear mixed (position and velocity) control mode to explain the open- and closed-loop responses of the HVS. It suggests possible neural correlates for the HVS, some of which are supported by existing data. A coarse disparity computation mechanism is sufficient to generate vergence movements. It is possible to explain the large delay (160 msec) seen in vergence responses by a combination of finite rise-time of membrane potential of pre-synaptic neurons and firing threshold of post-synaptic cells at various processing stages. The asymmetry in sensorimotor transformations can account for the asymmetric convergence and divergence dynamics. Due to nonleaky position integrators, our model does not exhibit the open-loop steady-state effect. On the other hand, regardless of the magnitude of the clamped disparity, our model predicts that the vergence system will continue to operate until its physiological limits. We have shown that the network model of the HVS proposed here is capable of explaining a wide range of short-term dynamical data under both closed- and open-loop conditions. The model also makes several novel and important predictions. It predicts that the vergence system would exhibit motor nonlinearity. It also predicts that the vergence errors are a result of asymmetry between the divergence and convergence sub-systems.

REFERENCES

Barlow, H. B., Blakemore, C. & Pettigrew, J. D. (1967). The neural mechanism of binocular depth discrimination. *Journal of Physiology, 193*, 327–342.

Carpenter, R. H. S. (1988). *Movements of the eyes*. London: Pion.

Crane, H. D. & Steele, C. M. (1978). Accurate three-dimensional eyetracker. *Applied Optics, 17*, 691–705.

Dev, P. (1975). Perception of depth surfaces in random-dot stereograms: A neural model. *International Journal of Man-Machine Studies, 7*, 511–528.

Duwaer, A. L. & van Den Brink, G. (1981). Diplopia thresholds and the initiation of vergence eye-movements. *Vision Research, 21*, 1721–1737.

Eckmiller, R. (1981). A model of neural network controlling foveal pursuit eye movements. In: *Progress in oculomotor research* (pp. 541–550). Amsterdam: Elsevier North Holland.

Erkelens, C. J., Van Der Steen, J., Steinman, R. M. & Collewijn, H. (1989a) Ocular vergence under natural conditions. II. Gaze-shifts between real targets differing in distance and direction. *Proceedings of the Royal Society, London, 236*, 441–465.

Erkelens, C. J., Van Der Steen, J., Steinman, R. M. & Collewijn, H. (1989b) Ocular vergence under natural conditions. I. Continuous changes of target distance along the median plane. *Proceedings of the Royal Society, London, 236*, 417–440.

Gamlin, P. D., Gnadt, J. W. & Mays, L. E. (1989). Abducen internuclear neurons carry an inappropriate signal for ocular convergence. *Journal of Neurophysiology, 62*, 70–81.

Gamlin, P. D. & Mays, L. E. (1992). Dynamic properties of medial rectus motoneurons during vergence eye movements. *Journal of Neurophysiology, 67*, 64–74.

Grossberg, S. (1988). Nonlinear neural networks: Principles, mechanisms, and architectures. *Neural Networks, 1*, 17–61.

Grossberg, S. & Kuperstein, M. (1989). *Neural dynamics of adaptive sensory-motor control*. New York: Pergamon Press.

Hering, E. (1868). *The theory of binocular vision*. New York: Plenum Press.

Hubel, D. H. & Wiesel, T. N. (1970). Cells sensitive to binocular depth in area 18 of macaque monkey cortex. *Nature, 255*, 41–42.

Hung, G. K. & Semmlow, J. L. (1980). Static behavior of accommodation and vergence: Computer simulation of interactive dual-feedback system. *IEEE Transactions on Biomedical Engineering, 27*, 439–447.

Hung, G. K., Semmlow, J. L. & Ciuffreda, K. J. (1986). A dual-mode dynamic model of the vergence eye movement system. *IEEE Transactions on Biomedical Engineering, 33*, 1021–1028.

Keller, E. L. (1981). Oculomotor neuron behavior. In: *Models of oculomotor behavior and control*. Florida: CRC Press.

Krishnan, V. V. & Stark, L. (1977). A heuristic model for human vergence eye movement system. *IEEE Transactions on Biomedical Engineering, 24*, 44–49.

Krishnan, V. V. & Stark, L. (1983). *Vergence eye movements: Basic and clinical aspects* Boston: K. J. Butterworths.

Livingstone, M. S. & Hubel, D. H. (1987). Psychophysical evidence for separate channels for perception of form, color, movement and depth. *Journal of Neuroscience, 7*, 416–3468.

Madox, E. E. (1907). *The clinical use of prisms; and the decentring of lenses*, 5th edn. Bristol: John Wright.

Marr, D. & Poggio, T. (1976). Cooperative computation of stereo disparity. *Science, 194*, 283–287.

Maunsell, J. H. R. & Van Essen, D. C. (1983). Functional properties of neurons in middle temporal visual area of the macaque monkey. II. Binocular interactions and sensitivity to binocular disparity. *Journal of Neurophysiology, 49*, 1148–1167.

Mays, L. E., Porter, J. D., Gamlin, P. D. R. & Tello, C. A. (1986). Neural control of vergence eye movements: Neurons encoding vergence velocity. *Journal of Neurophysiology, 56*, 1007–1021.

Mays, L. (1984). Neural control of eye movements: Convergence and divergence neurons in midbrain. *Journal of Neurophysiology, 51*, 1091–1108.

Nikara, T., Bishop, P. O. & Pettigrew, J. D. (1968). Analysis of retinal correspondence by studying receptive fields of binocular single units in cat striate cortex. *Experimental Brain Research, 6*, 353–372.

Öğmen, H. (in press). Sensorial nonassociative learning and its implications for visual perception. In: Omidvar, O. (Ed.), *Progress in neural nets*. New Jersey: Ablex.

Patel, S. S., Öğmen, H., White, J. M. & Jiang, B. C. (1996). Simulations of a human vergence system model. *Tech. rep. 96–06*. Houston: University of Houston, Systems Neural-Nets and Computing Technical Report.

Pettigrew, J. D., Nikara, T. & Bishop, P. O. (1968). Binocular interaction on single units in cat striate cortex: Simultaneous stimulation by single moving slits with receptive fields in correspondence. *Experimental Brain Research, 6*, 391–410.

Pobuda, M. & Erkelens, C. J. (1993). The relationship between absolute disparity and ocular vergence. *Biological Cybernetics, 68*, 221–228.

Poggio, G. F. & Ficher, B. (1977). Binocular interaction and depth sensitivity in striate and prestriate cortex of behaving rhesus monkeys. *Journal of Neurophysiology, 40*, 1392–1405.

Rashbass, C. & Westheimer, G. (1961a) Disjunctive eye movements. *Journal of Physiology, 159*, 339–360.

Rashbass, C. & Westheimer, G. (1961b) Independence of conjugate and disjunctive eye movements. *Journal of Physiology, 159*, 361–364.

Riggs, L. A. & Niehl, E. W. (1960). Eye movements recorded during convergence and divergence. *Journal of Optical Society of America, 50*, 913–920.

Robinson, D. A. (1970). Oculomotor unit behavior in the monkey. *Journal of Neurophysiology, 33*, 393–404.

Robinson, D. A. (1981). The use of control system analysis in neurophysiology of eye movements. *Annual Reviews of Neuroscience, 4*, 463–503.

Roy, J., Komatsu, H. & Wurtz, R. H. (1992). Disparity sensitivity of neurons in monkey extrastriate area MST. *The Journal of Neuroscience, 12*, 2478–2492.

Schor, C. M. (1979). The relationship between fusional vergence and fixation disparity. *Vision Research, 19*, 1359–1367.

Schor, C. M. (1980). Fixation disparity: A steady state error of disparity-induced vergence. *American Journal of Optometry and Physiological Optics, 57*, 618–631.

Schor, C. M. (1992). A dynamic model of cross-coupling between accommodation and convergence: Simulations of step and frequency responses. *Optometry and Vision Science, 69*, 258–269.

Semmlow, J. L., Hung, G. K. & Ciuffreda, K. J. (1986). Quantitative assessment of disparity vergence components. *Investigative Ophthalmology and Visual Science, 27*, 558–564.

Semmlow, J. L., Hung, G. K., Horng, J. & Ciuffreda, K. J. (1993). Initial control component in disparity vergence eye movements. *Ophthalmic Physiological Optics, 13*, 48–54.

Semmlow, J. L., Hung, G. K., Horng, J. L. & Ciuffreda, K. J. (1994). Disparity vergence eye movements exhibits preprogrammed motor control. *Vision Research, 34*, 1335–1343.

Sethi, B. (1986). Vergence adaptation: A review. *Documenta Opthalmologica, 63*, 247–263.

Westheimer, G. & Mitchell, A. M. (1956). Eye movement responses to convergence stimuli. *A.M.A. Archives in Ophthalmology, 55*, 848–856.

Westheimer, G. & Mitchell, A. M. (1969). The sensory stimulus for disjunctive movements. *Vision Research, 9*, 749–755.

Zuber, B. L. & Stark, L. (1968). Dynamical characteristics of the fusional vergence eye-movement system. *IEEE Transactions on Systems Science and Cybernetics, 4*, 72–79.

Acknowledgements—This material is based in part upon work supported by NIH Grants EY08862, MH49892, EY07551, and by the Texas Advanced Technology Program under Grant 003652023. We thank Dr Harold Bedell for helpful discussions and comments on the manuscript. We also thank all the subjects (LFH, NYN, and VTA) for their patience during the experiments; Drs L. Mays, J. L. Semmlow, and G. Westheimer for giving us the permission to reproduce their experimental data; and finally the reviewers for their detailed comments that helped improve the presentation of the manuscript.

APPENDIX A: MATHEMATICAL DESCRIPTION OF THE MODEL

The model uses additive and multiplicative (shunting) types of equations. For a general review of these equations and their relationship to biological neurons the reader is referred to Grossberg

(1988) (in particular Sections 6, 9, and 13–15). The velocity gate control cells make use of variable reaction-time property of shunting equations (rev. Öğmen, in press).

In the following equations the symbol x represents the "membrane potential" of the cells. The output of the cell is related nonlinearly to the membrane potential. This nonlinearity is denoted by $f()$. A simple linear-above-threshold function with saturation was used in all simulations:

$$f(x) = \begin{cases} 0 \text{ if } x < \Gamma \\ \alpha x \text{ if } \Gamma \le x < \Omega \\ \alpha\Omega \text{ if } \Omega \le x, \end{cases} \tag{A1}$$

where Γ, Ω, and α are constants determining the threshold, saturation, and gain of the firing function, respectively. The variables and parameters related to the left-eye (right-eye) are denoted by the superscript L (R). The variables and parameters for the convergence (divergence) circuits are denoted by the subscript $\Uparrow$ ($\Downarrow$). For simplicity, wherever possible only the equations, for the left eye and the convergence circuits are given. Those for the right eye and the divergence circuits are obtained by interchanging L and R, $\Uparrow$ and $\Downarrow$, respectively.

Normalized retinotopic map (NRM). Since the model does not address the stage of target selection, localization, and normalization, our description starts with the activities of neurons in the NRM. Let us denote the activity (membrane potential) of a neuron in this map by $x^{\mathrm{L}}_{\mathrm{NRM},i}$ where the subscript i denotes the retinotopic position of the cell. The retinotopic positions i range from $-N$ to N; with $i = 0$ corresponding to foveal position. The dynamics of the cells in the NRM are described by the additive equation

$$K_{\mathrm{s}} \frac{\mathrm{d}x^{\mathrm{L}}_{\mathrm{NRM},\,i}}{\mathrm{d}t} = -A^{\mathrm{L}}_{\mathrm{NRM},\,i} x^{\mathrm{L}}_{\mathrm{NRM},\,i} + I^{\mathrm{L}}_{i}, \tag{A2}$$

with $i = -N, -N+1, \ldots, -1, 0, 1, \ldots, N-1, N$. The first term on the right-hand side of the equation is a passive decay term. In this and the following equations the symbol A is used to denote a (positive) decay constant and K_{s} is a global scaling factor. The second term is the input to the neuron from the target selection, localization, and normalization stage. This input is set to:

$$I^{\mathrm{L}}_{i} = K_{\mathrm{i}}\delta(i - i^{\mathrm{L}}), \tag{A3}$$

where $\delta(.)$ is the Kronecker delta function, i^{L} is the retinal position of the target in the left eye and K_{i} is the amplitude of the input. Note that the $\delta(.)$ function is a simplification and in general we posit a distribution whose extent depends on the size of the target. This implies that the unsaturated peak vergence velocity will be higher for larger targets since a larger number of disparity coders would be activated. Most natural targets are larger compared to the laboratory targets and experiments with natural targets support this prediction (Erkelens *et al*., 1989b).

Map of disparity detectors (MDD). Disparity detectors are organized into a two-dimensional map as shown in Fig. 2. The horizontal axis of this map corresponds to different values of disparity. Let us denote this dimension by index d. More than one combination of inputs from the left and right NRMs can correspond to the same disparity. For each disparity value, neurons representing these different combinations are positioned along the vertical axis. Let index l denote this dimension. The dynamics of a disparity detector neuron positioned at (d, l) (i.e. combination l for disparity d) in the array is given by the additive equation

$$K_{\mathrm{s}} \frac{\mathrm{d}x_{\mathrm{DD},\,d,\,l}}{\mathrm{d}t} = -A_{\mathrm{DD},\,d,\,l} x_{\mathrm{DD},\,d,\,l} + f^{\mathrm{L}}_{\mathrm{NRM}}\left(x^{\mathrm{L}}_{\mathrm{NRM},\,l}\right) + F^{\mathrm{R}}_{\mathrm{NRM}}\left(x^{\mathrm{R}}_{\mathrm{NRM},\,d-l}\right), \tag{A4}$$

with $-2N \le d \le 2N$ and $\max(-N, d-N) \le l \le \min(\mathrm{N}, d+N)$. The inequality for d sets the limits for maximum and minimum possible disparity values. The inequality for l sets the range for different combinations that can yield a particular disparity value and generates the "diamond" shape of the disparity detector map. The synaptic weight for all synapses between the two NRMs and the disparity detectors is unity.

Map of disparity coders (MDC). The two-dimensional array of disparity detection is converted to a one-dimensional array of disparity by making those disparity detector neurons that are tuned to the same disparity converge to a single neuron. Such a convergence can be described by

$$K_{\mathrm{s}} \frac{\mathrm{d}x_{\mathrm{DC},\,d}}{\mathrm{d}t} = -A_{\mathrm{DC},\,d} x_{\mathrm{DC},\,d} + \sum_{l=\max(-N,\,d-N)}^{\min(N,\,d+N)} f_{\mathrm{DD}}(x_{\mathrm{DD},\,d,\,l}), \tag{A5}$$

with $-2N \le d \le 2N$. The limits of l set the range for different combinations in "diamond" topology that can yield a particular disparity d.

Velocity cells. For simplicity, we have used just two vergence velocity cells, one convergent and one divergent. As shown in Fig. 3, positive and negative disparities project respectively to convergence and divergence velocity cells. The dynamics of convergence and divergence velocity cells are described by the additive equations

$$K_{\mathrm{s}} \frac{\mathrm{d}x_{\mathrm{V}\Uparrow}}{\mathrm{d}t} = -A_{\mathrm{V}\Uparrow} x_{\mathrm{V}\Uparrow} + \sum_{d=0}^{2N} w_{d,\,\mathrm{V}\Uparrow} f_{\mathrm{DC}}(x_{\mathrm{DC},\,d}) \tag{A6}$$

and

$$K_{s} \frac{\mathrm{d}x_{\mathrm{V}\Downarrow}}{\mathrm{d}t} = -A_{\mathrm{V}\Downarrow} x_{\mathrm{V}\Downarrow} + \sum_{d=-2N}^{0} w_{d,\,\mathrm{V}\Downarrow} f_{\mathrm{DC}}(x_{\mathrm{DC},\,d}), \tag{A7}$$

where $w_{d,\,\mathrm{V}\Uparrow}$ and $w_{d,\,\mathrm{V}\Downarrow}$ are the weights whose strength is proportional to the position of the presynaptic neuron in the disparity map, i.e. proportional to d.

Position cells. The position signal is obtained by integrating the activity of the velocity cells. However, since the activity of velocity cells is always non-negative, an opponent input is required to discharge the integrator when the vergence demand changes from convergence to divergence or vice versa. This is achieved by push–pull integration dynamics described by:

$$K_{\mathrm{s}} \frac{\mathrm{d}x_{\mathrm{P}\Uparrow}}{\mathrm{d}t} = (B_{\mathrm{P}\Uparrow} - x_{\mathrm{P}\Uparrow}) w_{\mathrm{V}\Uparrow,\,\mathrm{P}\Uparrow} f_{\mathrm{V}\Uparrow}(x_{\mathrm{V}\Uparrow}) - (D_{\mathrm{P}\Uparrow} + x_{\mathrm{P}\Uparrow}) w_{\mathrm{V}\Downarrow,\,\mathrm{P}\Uparrow} f_{\mathrm{V}\Downarrow}(x_{\mathrm{V}\Downarrow}), \tag{A8}$$

where $w_{\mathrm{V}\Uparrow,\,\mathrm{P}\Uparrow}$ and $w_{\mathrm{V}\Downarrow,\mathrm{P}\Uparrow}$ are the weights between the convergence and divergence velocity cells and the convergence position cell, respectively. Note the absence of a passive decay term in this equation. This means that the integrator does not decay when the inputs are zero.

Velocity overdrive circuit

Velocity predictor cells (VP). These cells are tuned to provide a close estimate of the actual vergence velocity signal that will be generated a reaction time (*ca* 160 msec) later. The dynamics of the convergence velocity predictor cell is given by:

$$K_{\mathrm{s}} \frac{\mathrm{d}x_{\mathrm{VP}\Uparrow}}{\mathrm{d}t} = -A_{\mathrm{VP}\Uparrow} x_{\mathrm{VP}\Uparrow} + \sum_{i=-N}^{N} \left(w^{\mathrm{L}}_{i,\,\mathrm{VP}\Uparrow} f^{\mathrm{L}}_{\mathrm{NRM}}\left(x^{\mathrm{L}}_{\mathrm{NRM},\,i}\right) + w^{R}_{i,\,\mathrm{VP}\Uparrow} f^{R}_{\mathrm{NRM}}\left(x^{R}_{\mathrm{NRM},\,i}\right)\right). \tag{A9}$$

As illustrated in Fig. 4(b), the weights $w^{\mathrm{L}}_{i,\,\mathrm{VP}\Uparrow}$ and $w^{\mathrm{R}}_{i,\,\mathrm{VP}\Uparrow}$ are proportional to retinal eccentricity and, $w^{\mathrm{L}}_{i,\,\mathrm{VP}\Downarrow} = -w^{\mathrm{L}}_{i,\,\mathrm{VP}\Uparrow}$ and $w^{\mathrm{R}}_{i,\,\mathrm{VP}\Downarrow} = -w^{\mathrm{R}}_{i,\,\mathrm{VP}\Uparrow}$. Note that in the above equations, the superscripts L and R indicate the corresponding retinotopic map.

Velocity trigger cells (VT). These additive cells act as velocity level detectors in the VOCC, and are identical in every respect except their firing thresholds. The equation describing their dynamics is as below (assume for divergence):

$$K_{\mathrm{s}} \frac{\mathrm{d}x_{\mathrm{VT},\,i}}{\mathrm{d}t} = -A_{\mathrm{VT},\,i} x_{\mathrm{VT},\,i} + f_{\mathrm{VP}\Uparrow}(x_{\mathrm{VP}\Uparrow}) + f_{\mathrm{VP}\Downarrow}(x_{\mathrm{VP}\Downarrow}), \tag{A10}$$

with $i = 1, 2, 3$.

Velocity gate control cells (VG). These shunting cells provide a very critical feature of rapid turn-on and a slow turn-off that are needed to hold the VOGs off for a suitable period of time once they are inactivated by a sudden change in position. This property helps

eliminate any possibility of oscillations during step movements. The dynamics of these cells are described by:

$$K_s \frac{dx_{VG,i}}{dt} = -A_{VG} x_{VG,i} + \left(B_{VG} - x_{VG,i}\right) f_{VT,i}(x_{VT,i}), \qquad (A11)$$

with $i = 1, 2, 3$.

Velocity overdrive gate cells. These additive cells behave as switches that are turned off if the corresponding VGs are active. The dynamics of the VOG convergence cells are described by:

$$K_s \frac{dx_{VOG\Uparrow,i}}{dt} = -A_{VOG} x_{VOG\Uparrow,i} + f_{V\Uparrow}(x_{V\Uparrow}) - f_{VG}(x_{VG,i}), \qquad (A12)$$

with $i = 1, 2, 3$.

Velocity summer cells (VS). This additive cell adds the inputs from all the overdrive channels and the direct velocity channel, thus providing a variable velocity signal to the motoneuron/plant system based on the smoothness of the vergence stimulus. The dynamics of the VS convergence cell is described by:

$$K_s \frac{dx_{VS\Uparrow}}{dt} = -A_{VS\Uparrow} x_{VS\Uparrow} + w_{V\Uparrow,VS\Uparrow} f_{V\Uparrow}(x_{V\Uparrow}) + \sum_{i=1}^{3} w_{VOG\Uparrow,i,VS\Uparrow} f_{VOG}(x_{VOG\Uparrow,i}) \qquad (A13)$$

Active turn-off circuit

In order to understand the function of this circuit let us analyze the behavior of the model when no target is selected, i.e. when $I_i^L = I_i^R = 0$ for all i. An inspection of Eqs (A2), (A4), (A5), (A6) and (A7) shows that all activities in the NRM, map of disparity

TABLE B1. Cell characteristics

Cell type	A	Γ	α	Ω	B	D	R	K
NRM	1	0	0.1	10	N/A	N/A	N/A	10
MDD	1	1	1	1	N/A	N/A	N/A	N/A
MDC	1	0	1	1	N/A	N/A	N/A	N/A
V⇑	1	0	1	1	N/A	N/A	N/A	N/A
V⇓	1	0	1	1	N/A	N/A	N/A	N/A
P⇑	0	−0.475	1	1	0.5	0.5	N/A	N/A
P⇓	0	−0.5	1	1	0.5	0.5	N/A	N/A
VP	1	0	1	1	N/A	N/A	N/A	N/A
VT,1	1	0.003	1	1	N/A	N/A	N/A	N/A
VT,2	1	0.01	1	1	N/A	N/A	N/A	N/A
VT,3	1	0.03	1	1	N/A	N/A	N/A	N/A
VG	0.1	0.005	1	1	1	N/A	N/A	N/A
VOG	1	0	1	1	N/A	N/A	N/A	N/A
VS	1	0	1	5	N/A	N/A	N/A	N/A
AD	0.5	0.1	1	1	1	N/A	−0.2	N/A
AS⇑	1	0.475	1	1	N/A	N/A	N/A	N/A
AS⇓	1	0.5	1	1	N/A	N/A	N/A	N/A

TABLE 3. Plant characteristics

Subject	τ	KP⇑	KP⇓	KV⇑	KV⇓
LFH	25	2	2	0.2	0.2
NYN	25	2	2	0.06	0.06
VTA	25	2.2	2.2	0.05	0.05

TABLE 2. Synaptic weights

Cell type	Subject	Weight variable	Weights
V⇑	LFH	d, V⇑	(0, 0), (1, 0.075), (2, 0.075), (3, 0.15), (4, 0.25), (5, 0.4), (6, 0.6), (7, 0.8), (8, 1)
V⇑	NYN	d, V⇑	(0, 0), (1, 0.025), (2, 0.15), (3, 0.25), (4, 0.5), (5, 1.4), (6, 2), (7, 2.8), (8, 3.6)
V⇑	VTA	d, V⇑	(0, 0), (1, 0.07), (2, 0.1), (3, 0.3), (4, 0.8), (5, 1.4), (6, 2), (7, 2.8), (8, 3.6)
V⇓	LFH	d, V⇓	(0, 0), (−1, 0.075), (−2, 0.12), (−3, 0.45), (−4, 0.7), (−5, 1.4), (−6, 2), (−7, 2.8), (−8, 3.6)
V⇓	NYN	d, V⇓	(0, 0), (−1, 0.025), (−2, 0.15), (−3, 0.4), (−4, 0.8), (−5, 1.4), (−6, 2), (−7, 2.8), (−8, 3.6)
V⇓	VTA	d, V⇓	(0, 0), (−1, 0.07), (−2, 0.1), (−3, 0.3), (−4, 0.8), (−5, 1.4), (−6, 2), (−7, 2.8), (−8, 3.6)
P⇑	*−VTA	V⇑, P⇑	0.02
P⇑	VTA	V⇑, P⇑	0.015
P⇑	*−VTA	V⇓, P⇑	−0.02
P⇑	VTA	V⇓, P⇑	−0.015
P⇑	*	S⇓, P⇓	0.1
P⇑	*	S⇑, P⇑	−0.1
P⇓	*−VTA	V⇑, P⇓	−0.02
P⇓	VTA	V⇑, P⇓	−0.01
P⇓	*−VTA	V⇓, P⇑	0.02
P⇓	VTA	V⇓, P⇓	0.015
P⇓	*	S⇓, P⇓	−0.1
P⇓	*	S⇑, P⇓	0.1
VP⇑	*	i^L, VP⇑	(4, 0.3), (3, 0.225), (2, 0.15), (1, 0.075), (0, 0), (−1, −0.75), (−2, −0.15), (−3, −0.225), (−4, −0.3)
VP⇑	*	i^R, VP⇑	(4, 0.3), (3, 0.225), (2, 0.15), (1, 0.075), (0, 0), (−1, −0.075), (−2, −0.15), (−3, −0.225), (−4, −0.3)
VS⇑	*	V⇑, VS⇑	1.5
VS⇑	*	VOG⇑, i, VS⇑	(1, 1.5), (2, 1.5), (3, 1.5)
VS⇓	*	V⇓, VS⇓	0
VS⇓	*	VOG⇓, i, VS⇓	(1, 1.5), (2, 1.5), (3, 3)
S⇑	*	AD, S⇑	10
S⇓	*	AD, S⇓	10

detectors, map of disparity coders, as well as the activities of velocity cells will decay to 0. Substituting $f_{V\Uparrow}(x_{V\Uparrow}) = f_{V\Downarrow}(x_{V\Downarrow}) = 0$ in Eq. (A8) shows that $\frac{dx_{P\Uparrow}}{dt} = 0$, correspondingly $\frac{dx_{P\Downarrow}}{dt} = 0$. Therefore, since the derivative of position does not change, the eyes will stay where they are. In order to return the eyes to their resting position, we introduce an active circuit that detects the absence of a binocular target. A simple way of doing this is to summate all the activities in the disparity coders:

$$K_s \frac{dx_{AD}}{dt} = -A_{AD}\left(x^L_{AD} - R_{AD}\right) + (B_{AD} - x_{AD}) \sum_{i=-2N}^{2N} w_{DC,i,AD} f_{DC}(x_{DC,i}), \quad \text{(A14)}$$

where x_{AD}, R_{AD} is the activity of the "activity detector" neuron (ADN) and its resting level, respectively. All the synapses between the disparity coders and ADN have unity strength. In order to dictate the resting positions of the eyes we introduce a "switch" neuron (SWN) that moves the eyes when there is no selected target and the eyes are in a position different from their resting positions. The dynamics of switch cells are described by:

$$K_s \frac{dx_{S\Uparrow}}{dt} = -A_{S\Uparrow} x_{S\Uparrow} + w_{P\Uparrow,\,S\Uparrow} f_{P\Uparrow}(x_{P\Uparrow}) - w_{AD,\,S\Uparrow} f_{AD}(x_{AD}), \quad \text{(A15)}$$

where $x_{S\Uparrow}$ is the activity of the convergence switch cell. $w_{P\Uparrow,\,S\Uparrow}$ is the synaptic weight between convergence position cell and the convergence SWN. $w_{AD,\,S\Uparrow}$ is the weight between the ADN and the convergence SWN. Since the switch cells control the position of the eyes, Eq. (A8) is modified as follows:

$$K_s \frac{dx_{P\Uparrow}}{dt} = \left(B_{P\Uparrow} - x_{P\Uparrow}\right)\left[w_{V\Uparrow,\,P\Uparrow} f_{V\Uparrow}(x_{V\Uparrow}) + w_{S\Downarrow,\,P\Uparrow} f_{S\Downarrow}(x_{S\Downarrow})\right] - \left(D_{P\Uparrow} + x_{P\Uparrow}\right)\left[w_{V\Downarrow,\,P\Uparrow} f_{V\Downarrow}(x_{V\Downarrow}) + w_{S\Uparrow,\,P\Uparrow} f_{S\Uparrow}(x_{S\Uparrow})\right]. \quad \text{(A16)}$$

Motoneurons and the plant

The entire system of motoneurons and the eye plant is implemented as a first order system (Robinson, 1981; Krishnan & Stark, 1983; Gamlin & Mays, 1992). The differential equation for this system is:

$$K_p \frac{d\theta^L}{dt} = -\frac{1}{\tau^L}\theta^L + K^L_{P\Uparrow} f_{P\Uparrow}(x_{P\Uparrow}) - K^L_{P\Downarrow} f_{P\Downarrow}(x_{P\Downarrow}) + K^L_{V\Uparrow} f_{VS\Uparrow}(x_{VS\Uparrow}) + K^L_{V\Downarrow} f_{VS\Downarrow}(x_{VS\Downarrow}), \quad \text{(A17)}$$

where θ^L, τ, $K_{P\Uparrow}$, $K_{P\Downarrow}$, $K_{V\Uparrow}$, and $K_{V\Downarrow}$ are respectively the position of the left eye in degrees, the time constant, convergence and divergence position and velocity gains, respectively, of the system. K_p is a global scaling constant.

APPENDIX B: SIMULATION METHODS

The model consists of the system of differential equations described by Eqs (A1)–(A17). For simulations, the system was solved numerically using the fixed-step (5 msec) Runge–Kutta 3–4 formula. The global scaling factors K_s and K_p were 0.05 and 0.005, respectively. The parameters that are different for NYN and VTA compared to LFH are tagged with their names. The parameters that are untagged are for all the subjects. The simulation software was written in ANSI C and all the simulations were performed on a Macintosh II computer equipped with a Daystar 50 MHz 68030 accelerator. The parameters used for the simulations are listed in Table B1. Parameters without reference to a subject (*) are applicable to all subjects. In some cases the phrase "*xxx" is used to mean all subjects except xxx. Wherever applicable, the unspecified parameters of the right eye are the same as those of the left eye. Details of simulation procedures are given in Patel *et al.*, (1996) and a copy of the simulation software can be obtained from the authors.